ADVANCED FUNCTIONAL MATERIALS
www.afm-journal.de

Interlayer Electron Redistribution Engineering for Ultralow Friction in 2D Electrides

*Jingcheng Qi, Giuliana Materzanini, Gian-Marco Rignanese, Maria Clelia Righi, and Junjie Wang**

Friction accounts for up to 30% of global energy consumption, underscoring the urgent need for superlubricity in advanced materials. 2D electrides feature cationic layers separated by 2D confined anionic electrons. Ab initio calculations reveal that interlayer friction correlates with cationic charge and sliding-induced charge redistribution. Remarkably, the 2D electride Ba_2N exhibits lower interlayer friction than graphene despite stronger interlayer adhesion, contradicting conventional tribological understanding. This anomaly stems from electron redistribution serving as the dominant energy dissipation pathway. Deep potential molecular dynamics (DPMD) simulations show that incommensurate twisted interfaces ($2° < \theta < 58°$) in Ba_2N achieve structural superlubricity by suppressing out-of-plane buckling and energy corrugation. Notably, a critical normal load of 2.3 GPa enables barrier-free sliding in commensurate Ba_2N ($\theta = 0°$), with an ultralow shear-to-load ratio of 0.001, suggesting superlubricity potential. Furthermore, electron doping effectively reduces interlayer friction by controllably modulating stacking energies. These findings establish 2D electrides as a transformative platform for energy-efficient tribology, enabling scalable superlubricity through twist engineering, load adaptation, or electrostatic gating. This work advances the fundamental understanding of electron-mediated friction, with Ba_2N serving a model for cost-effective, high-performance material design.

1. Introduction

Friction, a widespread physical phenomenon, frequently results in undesirable consequences such as wear failures and energy loss across industries, with research suggesting that up to 30% of energy consumption can be attributed to it.[1,2] Consequently, significant efforts have been directed toward minimizing friction and achieving "superlubricity", characterized by extremely low friction values. In 2004, Frenken et al. experimentally demonstrated superlubricity in graphite.[3] They observed that frictional forces between a graphite sheet and a highly oriented pyrolytic graphite (HOPG) crystal surface are significant only when the graphite sheet has a commensurate orientation relative to the HOPG substrate. In contrast, friction is significantly reduced for incommensurate orientations, a phenomenon referred to as "structural lubricity".[4] Superlubricity was also achieved in commensurate contacts by applying specific external loads and strains.[5–7] Researchers continue to explore new materials and approaches that offer increased stability and reduced cost for achieving superlubricity.[8–15]

In atomic force microscopy (AFM) measurements, friction primarily originates from the out-of-plane motion, which stems from the ultralow interlayer adhesion in van der Waals (vdW) interface.[16,17] Hence, enhancing substrate adhesion is key to reducing friction by suppressing out-of-plane wrinkling.[18,19] It is essential to find materials that simultaneously possess high interlayer adhesion and low shear strength. 2D electrides, characterized by cationic layers hosting interlayer electrons (**Figure 1a**), have garnered interest for their potential applications in various fields.[20–22] The alternating cationic layers and interlayer electrons allow for a high interlayer binding energy than graphene (e.g., 1.11 J m^{-2} for Ca_2N and 0.31 J m^{-2} for graphite),[23] but a considerable separation (e.g., 3.85 Å in Ca_2N),[21] comparable to typical vdW distances.[24] Moreover, the high-density interlayer electrons exhibit remarkable activity, making it convenient to control their distribution. Previous studies on both Ca_2N bilayers and bulk materials have demonstrated that their electronic structure remains insensitive to stacking arrangements.[25] This phenomenon was simply attributed to the effective screening of cationic layers by interlayer electrons, which minimizes interlayer charge variations during sliding. However, it remains unclear whether a superlubricity state can be induced in 2D electrides. While previous studies have focused on charge screening effects, the fundamental relationship between electron redistribution, energy barriers, and

J. Qi, G.-M. Rignanese, J. Wang
State Key Laboratory of Solidification Processing
Northwestern Polytechnical University
Xi'an 710072, P. R. China
E-mail: wang.junjie@nwpu.edu.cn
G. Materzanini, G.-M. Rignanese
Institute of Condensed Matter and Nanoscicences (IMCN)
Université Catholique de Louvain
Louvain-la-Neuve 1348, Belgium
G.-M. Rignanese
WEL Research Institute
Avenue Pasteur 6, Wavre 1300, Belgium
M. C. Righi
Department of Physics and Astronomy
University of Bologna
Bologna 40127, Italy
The ORCID identification number(s) for the author(s) of this article can be found under https://doi.org/10.1002/adfm.202525865

DOI: 10.1002/adfm.202525865

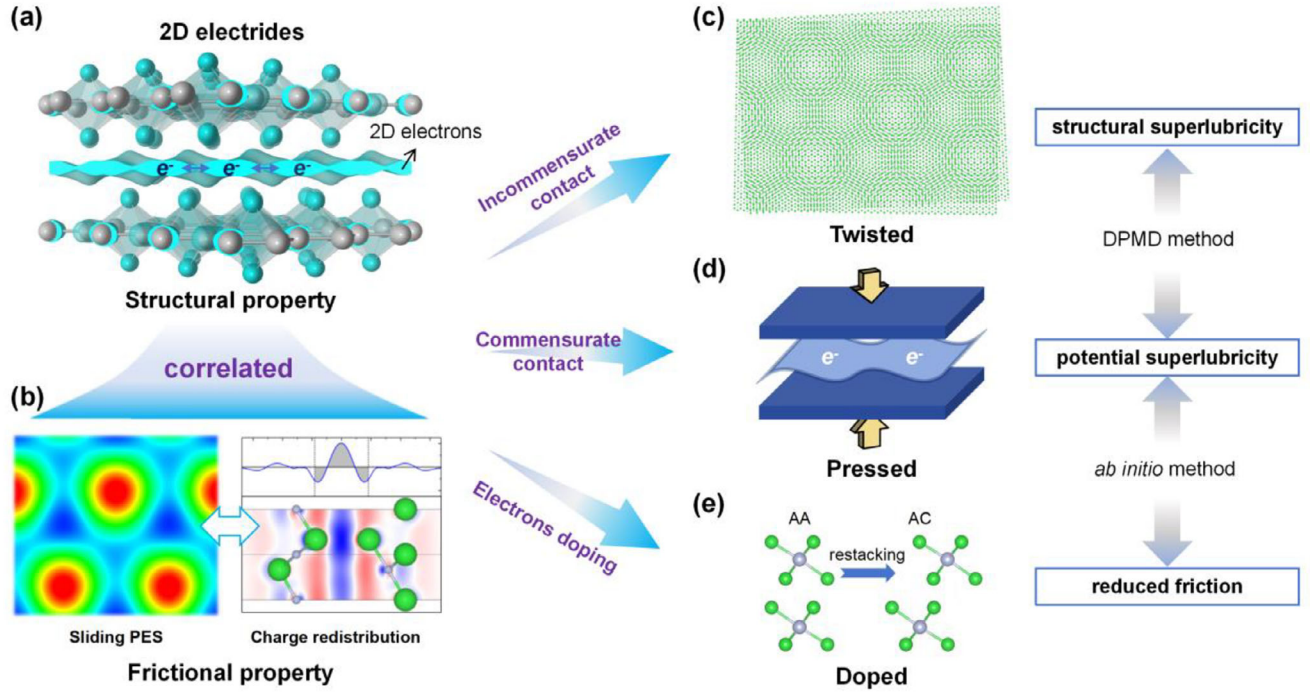

Figure 1. Investigation of intrinsic frictional properties and friction-reduction strategies in 2D electrides. a) Interlayer structure of 2D electrides characterized by localized 2D electrons distributed between two cationic layers. b) Sliding PES and interlayer charge redistribution are employed to describe the influence of sliding processes on interlayer interactions. c) Twisting-induced incommensurate contact of superlattice leads to structural superlubricity. d) Out-of-plane pressure causes collapse of the sliding energy barrier, resulting in ultralow friction. e) Electron-doping-induced interlayer restacking reduces the interlayer friction.

friction dynamics remains unexplored. This knowledge gap motivates our systematic investigation of the friction behavior in 2D electrides.

In this study, we conduct ab initio calculations to thoroughly investigate the frictional properties of 2D electrides by analyzing their sliding potential energy surfaces (PES). We identify the crucial role of structural parameters and charge redistribution in determining the interlayer friction of layered electrides (Figure 1b). Surprisingly, the Ba_2N bilayer exhibits significantly lower intrinsic friction than graphite. Our deep potential molecular dynamics (DPMD) simulations demonstrate that suitable twist angles ($2° < \theta < 58°$) can effectively suppresses the out-of-plane deformation in Ba_2N bilayer, enabling structural superlubricity (Figure 1c). Moreover, the commensurate ($\theta = 0°$) Ba_2N exhibits ultralow interlayer friction under an extra normal load, with the ratio between the shear strength and normal load reaching 0.001, highlighting its potential for superlubricity (Figure 1d). Additionally, electron doping effectively lowers the interlayer friction in 2D electrides by modulating the energy differences between various stacking configurations (Figure 1e).

2. Structural and Frictional Properties of 2D Electrides

We investigate a series of M_2X compounds with the anti-$CdCl_2$ structure (space group *R-3m*, #166), using alkaline-earth cations (M = Ca, Sr, and Ba) and nonmetal V-A elements (X = N, P, and As) as anions. Electrides like Ca_2N[21] and Ba_2N[26] have been confirmed experimentally, while others, such as Sr_2N, Sr_2P, Ba_2P, and Ba_2As have been predicted as stable 2D electrides through ab initio calculations.[27,28] Although Ca_2P, Ca_2As, and Sr_2As are thermodynamically metastable,[27] they are included for comparison. We fully optimize the conventional bulk unit cells of these compounds (**Figure 2a**), obtaining relaxed geometries and binding energies in agreement with previous reports (see Table S1, Supporting Information). The crystal structures feature three distinct layers, each composed of two atomic planes of M cations and one atomic plane of X anions. These layers are denoted as A, B, and C. The electron localization function (ELF) is calculated to visualize the electron distribution in the layers, with that of Ca_2N shown in Figure 2a. The interlayer electron sheets, spaced ≈6.33 Å apart, show negligible interaction, thus a bilayer model—consisting of a single electron sheet flanked by two cationic layers and vacuum—adequately represents their bonding and frictional properties. Figure S1 (Supporting Information) illustrates bilayer configurations with AB and AC stackings, related to one another by sliding the layers in the *x*-*y* plane, as detailed in the Supporting Information. For a general M_2X compound, the bilayer configurations are constructed as follows: the atomic (*x*, *y*, *z*) coordinates of the lower layer are fixed, while in the upper layer, the *z*-coordinates are held at the values corresponding to the minimum-energy stacking configuration. The (*x*, *y*) coordinates of the upper layer are then rigidly displaced by a vector (x^*, y^*) relative to the minimum-energy configuration.

We calculate the sliding PES per area, $\Delta E_{(x^*,\ y^*)}$, defined as:

$$\Delta E_{(x*,\ y*)} = \left(E_{(x*,\ y*)} - E_{(0,\ 0)}\right)/A \quad (1)$$

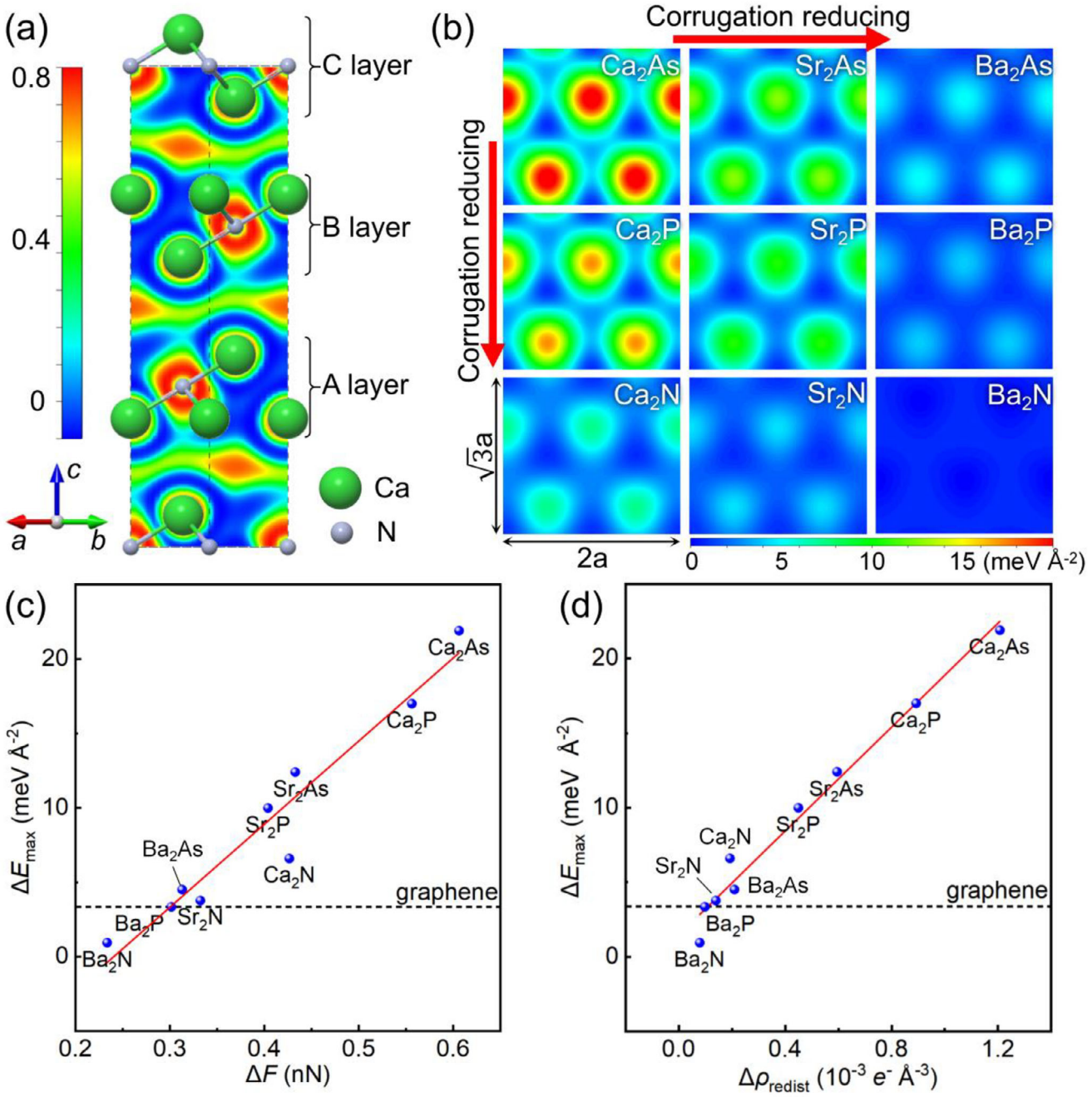

Figure 2. a) Side view of the bulk unit cell of Ca_2N electride with the calculated ELF. b) Calculated 2D PESs for the sliding of nine M_2X electrides in bilayer form. c) Linear correlation between the sliding energy barrier ΔE_{max} of M_2X bilayers and the Coulombic repulsion difference ΔF of nearest cations between the minimum- and maximum-energy configurations. d) Linear correlation between ΔE_{max} and the interlayer average charge redistribution ($\Delta\rho_{redist}$).

where $E_{(x^*,\ y^*)}$ and $E_{(0,\ 0)}$ are the total energies of the (x^*, y^*)-displaced configuration and the minimum-energy stacking configuration, respectively, and A is the xy unit cell area. Contour plots of $\Delta E_{(x^*,\ y^*)}$ for the nine M_2X bilayer models are shown in Figure 2b. These PESs exhibit periodicity in the 2D (x^*, y^*) displacement during sliding. Additionally, the PES for bilayer graphene is calculated for comparison (Figure S2, Supporting Information). The arrangement of these PESs in Figure 2b reflects a trend in which the electronegativity of the cations and anions decreases horizontally from left to right and vertically from bottom to top, respectively. In tribology, an important metric is the maximum energy barrier during sliding, ΔE_{max}, defined as the difference between the maximum and minimum energy per unit area along the sliding trajectory, i.e., the maximum value of $\Delta E_{(x^*,\ y^*)}$. As we move toward the lower right corner (Ba_2N bilayer), the PES becomes smoother, with a corrugation amplitude (ΔE_{max}) as low as 0.95 meV $Å^{-2}$, significantly lower than the value of 3.36 meV $Å^{-2}$ for the graphene bilayer. Moreover, the

calculated ΔE_{max} shows a notable dependence on the ionic size ratio ($R_{X/M}$) between the anion X and the cation M. M_2X bilayers with smaller $R_{X/M}$ values exhibit smaller ΔE_{max} (Figure S3 and Table S1, Supporting Information). Notably, when the ionic size ratio drops below 1.3 (e.g., for Ba_2N), the calculated ΔE_{max} is lower than that of the graphene bilayer.

We examine the correlation between ΔE_{max} and ΔF, where ΔF represents the difference in Coulombic repulsion between the two cationic layers in their minimum- and maximum-energy configurations. This repulsion is expressed as $F = kQ^2/d^2$, where k is the Coulomb's constant, d denotes the shortest distance between two cations in adjacent layers, and Q is the net charge of the cations, determined through Bader charge analysis (see Table S2, Supporting Information).[29,30]

The Bader method considers the zero-flux surface of the charge density to divide the molecular space into atomic volumes known as Bader basins. In electrides, the volume of the Bader basin around the interlayer anionic electrons where the electron density is maximum, known as a non-nuclear attractor, is estimated to be an empty sphere (pseudo atom). We perform Bader charge analysis on the pre-converged total charge density, referencing the projected charge density and employing a pseudo atom to account for interlayer anionic electrons. Additional computational details are provided in the Supporting Information. Using this approach, we identify the minimum- and maximum-energy configurations across various M_2X bilayers, and the Coulombic repulsion difference ΔF can be derived from the geometric relationship between adjacent cations:

$$\Delta F = kQ^2 \left(\frac{1}{{z_0}^2} - \frac{1}{a^2/3 + {z_0}^2} \right) \quad (2)$$

We observe a strong linear correlation (Pearson correlation coefficient 0.97) between ΔF and ΔE_{max} for the nine M_2X bilayers, as depicted in Figure 2c. This straightforward model provides a convenient method for predicting the frictional properties of anti-$CdCl_2$ 2D electrides based on the net charge of the cations (Q) and intrinsic structural factors (a, z_0).

Ultralow friction energy barriers in layered materials typically arise from weak interlayer interactions.[31,32] However, in Ba_2N electride, the adhesion energy between consecutive layers significantly exceeds that of graphite (48.06 compared to 16.96 meV $Å^{-2}$, see Table S1, Supporting Information), suggesting a crucial role for interlayer electrons in 2D electride sliding. It has been proposed that energy corrugation in friction originates from the non-uniform distribution of charge density in the interface region or from the evolution of charge density in dynamic stacking configurations.[33–37] Consequently, we conduct a detailed analysis of the relationship between the redistribution of interlayer electrons and the sliding energy barrier. To quantify the accumulation of interlayer electrons, we compute the difference between the total charge density ρ_{tot} of the M_2X bilayer and the sum of the charge densities ρ_{upp} and ρ_{low} of the isolated upper and lower layers: $\rho_{diff} = \rho_{tot} - (\rho_{upp} + \rho_{low})$. Contour plots of ρ_{diff} for the Ca_2N bilayer are shown in Figure S4 (Supporting Information). Charge density profiles along z, calculated by integrating ρ_{diff} over the surface area of the simulation cell A, reveal significant charge transfer from the cationic layers to the interlayer region upon bilayer formation. We evaluate the amount of interlayer charge redistribution ρ_{redist},[31] by integrating $\rho_{diff,xy}(z)$ over the interlayer region (z_0, Figure S1, Supporting Information) and normalizing by the interlayer volume:

$$\rho_{redist} = \frac{1}{Az_0} \int_{\frac{z_0}{2}}^{-\frac{z_0}{2}} \left| \rho_{diff,xy}(z) \right| dz \quad (3)$$

We investigate the impact of the different stacking configurations on $\rho_{diff,xy}(z)$ by computing the interlayer charge evolution upon sliding $\Delta\rho_{redist}$, i.e., the difference between ρ_{redist} in the minimum- and maximum-energy stacking configurations. Figure 2d shows ΔE_{max} as a function of $\Delta\rho_{redist}$ for the nine M_2X electrides, along with a linear fit showing a high Pearson correlation coefficient of 0.99. This indicates a strong correlation between the interlayer charge evolution and energy barriers upon sliding. Notably, all values of $\Delta\rho_{redist}$ are positive, indicating an increase in interlayer charge redistribution as the bilayer transitions from the minimum- to the maximum-energy stacking configuration. The higher the increase in the interlayer charge redistribution, the larger the energy barrier generated during sliding, and vice versa. Consequently, Ba_2N, with the smallest sliding energy barrier, exhibits the lowest increase in interlayer charge redistribution. The observed correlation between $\Delta\rho_{redist}$ and ΔE_{max} suggests that electron redistribution acts as the primary energy dissipation pathway during sliding. These findings offer valuable insights into leveraging the interlayer electrons of 2D electrides to tune their frictional properties.

3. Inducing Superlubricity in 2D Electrides through Incommensurate Contact

Previous research indicates that interlayer friction in rigid crystal interfaces can be influenced by lattice mismatch.[10,13,38] Misaligned lattices persist during sliding, leading to reduced energy corrugation. Although lattice mismatch can be quantified using geometric descriptors, other significant effects accompanying lattice twisting, such as in-plane/out-of-plane elastic deformations and thermal corrugation, are often overlooked. Although ab initio simulations can capture these phenomena, they are computationally prohibitive for large systems. To address the challenge of simulating moiré superlattices containing over 10 000 atoms, we adopted the DeePMD-kit framework,[39,40] utilizing interatomic forces generated by neural networks trained on ab initio data. This approach achieves the density functional theory (DFT) level accuracy and has been validated in large systems containing ≈11 000 atoms per moiré unit cell.[41,42] Our machine learning force field (MLFF) demonstrates high accuracy with force and energy errors below 58 meV $Å^{-2}$ and 3 meV per atom, respectively (Figure S5, Supporting Information), enabling direct simulation of twisted bilayer Ba_2N's dynamic behavior.

We construct 194 distinct Ba_2N bilayer models with twist angles ranging from 0° to 60° using coprime integer pairs (m, n) to define twisted superlattices through rotational stacking of monolayers (Figure S6, Supporting Information). Figure S7 (Supporting Information) displays the interlayer 2D ELF profiles of twisted bilayer Ba_2N at twist angles of 0°, 13.17°, 21.79°, and 27.80°, viewed along the [001] direction. Structural twisting causes a rearrangement of Ba atoms, resulting in a pronounced

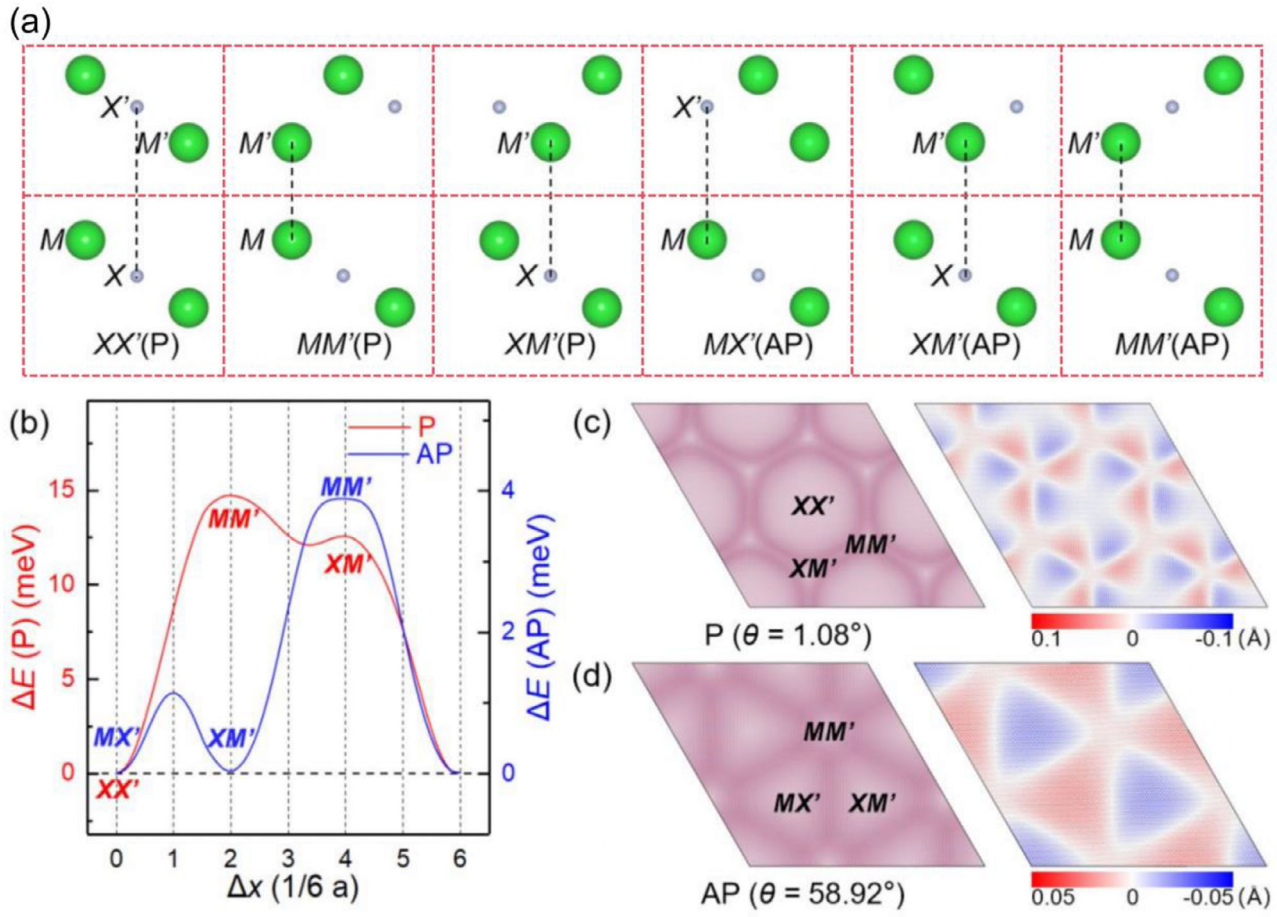

Figure 3. a) Schematic representation of the typical stacking configurations of bilayer Ba_2N with twist angles of 0° and 60°. The green and cyan balls represent Ba and N atoms, respectively. b) Energy variation of typical stacking configurations during sliding of the bilayer. The sliding direction is along the parallel (P) or antiparallel (AP) orientations of the initial bilayers. c) Moiré patterns (left) and color maps of the *z*-coordinate of the atoms (right) in one cationic layer of relaxed Ba_2N superlattices with twist angles of 1.08° and d) 58.92°. The color scheme for the maps of *z*-coordinate ranges from red (0.1 Å in (c) or 0.05 Å in (d)) to blue (−0.1 Å (c) or −0.05 Å (d)).

enhancement in the distribution of interlayer localized electrons (red regions with $ELF_{max} > 0.7$). To quantitatively assess the uniformity of this localization, the areal density of interlayer localized electrons is defined as the number of in-plane ELF maxima ($ELF_{max} > 0.7$) per unit area. As shown in Figure S7e (Supporting Information), this areal density increases substantially upon twisting, indicating a more homogeneous distribution of localized electrons. Such uniformity contributes to a flatter potential energy surface, thereby reducing the interlayer sliding barriers. These results demonstrate that the characteristic interlayer electron localization in 2D electrides is not only preserved but further enhanced by structural twisting.

At a twist angle of 60° (antiparallel-stacked, AP), the alignment of the two atomic layers in the bilayer model is opposite to that of the initial structure at 0° (parallel-stacked, P). The stacking configurations during interlayer sliding for both stacking orientations are illustrated in **Figure** 3a. Each configuration is labeled according to the pair of atoms facing each other across the interface, with the initial configuration denoted as XX'(P). The interlayer sliding energy profiles for both P (0°) and AP (60°) stacking orientations are calculated using first-principles methods. As shown in Figure 3b, the energy barriers differ significantly: 15 meV for P and only 4 meV for AP. This reduction in the AP case is attributed to the unique alignment of cationic sublayers, where opposing lattice vectors effectively cancel out periodic potential mismatches, leading to a flatter sliding PES. The AP stacking orientation also minimizes the Coulombic repulsion between the cationic layers. Notably, the P stacking orientation features two high-energy configurations (MM'(P) and XM'(P)), while the AP stacking orientation exhibits two nearly degenerate low-energy configurations (MX'(AP)) and (XM'(AP)). These stacking-dependent energy variations are critical for understanding the energetics and structural stability of twisted superlattices.

The relaxed structures of Ba_2N bilayers with small twist angles ($0° < \theta < 2°$ and $58° < \theta < 60°$) reveal prominent bright domains characterized by dislocation networks (Figure 3c,d). In the bilayer with P orientation and a small twist angle ($\theta = 1.08°$, left panel of Figure 3c), the lattice reconstructs into a hexagonal array of stacking domains (XX'(P)), which are separated by dislocation networks alternating between high-energy configurations (MM'(P)

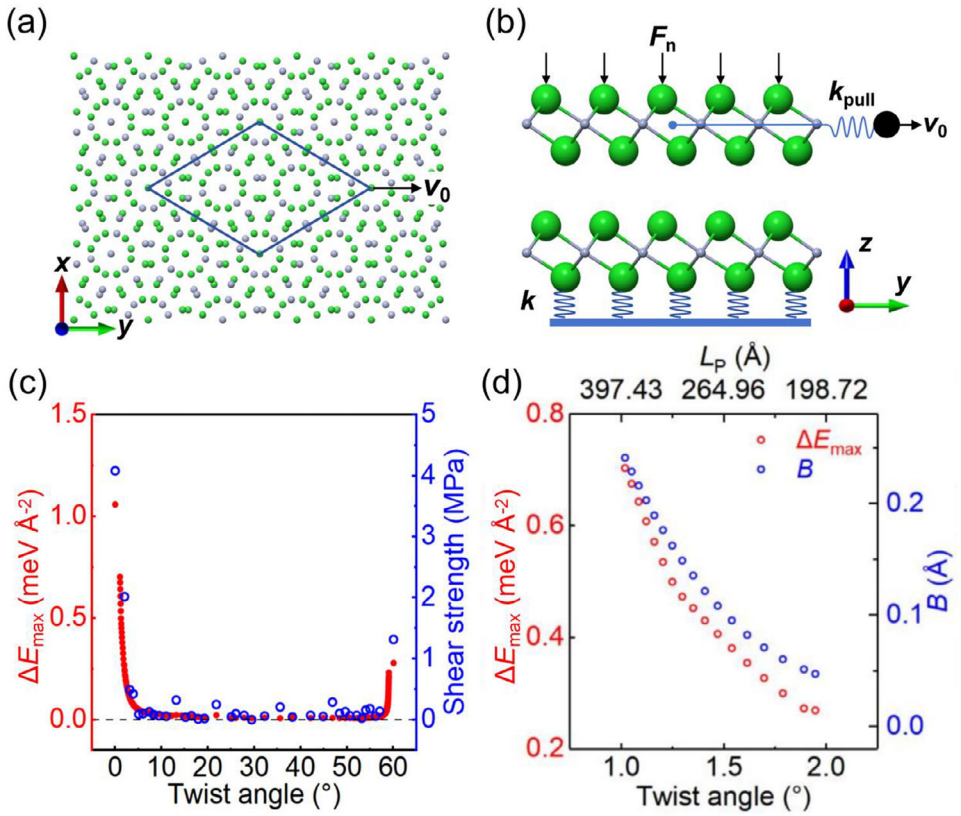

Figure 4. a) Top view of the bilayer Ba_2N model for a twist angle of $\theta = 21.79°$; b) Schematic illustration of the simulation setup: Basal Ba atoms in the substrate layer are fixed by springs with elastic constant k to maintain their initial positions. A virtual atom (black sphere) connects to the sliding layer through a spring (elastic constant k_{pull}), moving with a constant velocity v_0 parallel to the sliding direction. Ba and N atoms are represented by green and blue spheres, respectively. c) Sliding energy barrier ΔE_{max} (red dots) and shear strength (blue dots) of bilayer Ba_2N as a function of the twist angle in the range $0° < \theta < 60°$. d) Sliding energy barrier ΔE_{max} (red circles) and out-of-plane buckling B (blue circles) of bilayer Ba_2N for small twist angles in the range $0° < \theta < 2°$.

and XM'(P)). Conversely, in the bilayer with AP orientation and a small twist angle ($\theta = 58.92°$, left panel of Figure 3d), each moiré supercell contains two triangular domains corresponding to low-energy configurations (MX'(AP) and XM'(AP)), while the dislocation networks adopt the high-energy configuration (MM'(AP)). This overall tendency toward low-energy states drives the expansion of bright domains outwards from low-energy centers. Furthermore, at small twist angles, the mismatch between adjacent low-energy domains leads to the accumulation of dislocations in intermediate high-energy regions, forming dislocation walls that separate the domains.

Moreover, the enlargement of low-energy areas causes atomic layers to buckle out of plane uniformly across all layers in bilayer structures, regardless of the twist angle. The distribution of these buckles is influenced by perfect domains and dislocation networks. In the P orientation bilayer structure ($\theta = 1.08°$, right side of Figure 3c), a hexagonal domain is divided into six separate triangular buckles, distributed alternately near the domain walls. Conversely, in the AP orientation bilayer structure ($\theta = 58.92°$, right side of Figure 3d), two equally sized triangular domains in low-energy configurations MX'(AP) and XM'(AP) exhibit opposite out-of-plane buckling. No buckling is observed in the atomic layers atop the dislocation network in either scenario. These buckling patterns, which are influenced by low-energy perfect domains and high-energy dislocation networks, significantly affect the frictional properties of the bilayers.

For dynamic friction analysis, we perform molecular dynamic simulations on 36 selected representative models (Figure S8, Supporting Information). The twist angles and lattice constants of these 36 models are listed in Table S3 (Supporting Information). **Figure** 4a shows the characteristic lattice structure at $\theta = 21.79°$. Figure 4b shows the simulation setup: spring-based constraints are applied to the basal layer atoms of the substrate. The sliding layer is connected to a virtual atom moving at $v_0 = 10$ m s^{-1} along the lattice diagonal (Figure 4a). A uniform normal load is applied to each top Ba atom of the sliding layer. For all systems, constant-temperature molecular-dynamics simulations are performed for 1 ns at 300 K using a Nose-Hoover thermostat. The frictional performance is evaluated through the calculation of the lateral shear strength ($\tau = F_k/A$), where F_k represents the time-averaged kinetic friction force and A denotes the contact area. The calculated shear strengths τ of the 36 models are listed in Table S3 (Supporting Information).

Figure 4c presents the dependence of the maximum energy barriers (ΔE_{max}) and lateral shear strengths (τ) on the twist angles under zero normal load conditions. Commensurate lattices at $\theta = 0°$ and 60° exhibit energy barriers of 1.06 and 0.28 meV Å^{-2}, respectively. These barriers undergo a dramatic reduction

within two narrow range of twist angles ($0° < \theta < 2°$ and $58° < \theta < 60°$), collapsing to ultralow values (< 0.25 meV Å^{-2}) across incommensurate angles ($2° < \theta < 58°$), which strongly suggests the presence of structural superlubricity. This behavior mirrors the observed shear strength reduction approaching 0° and 60°, demonstrating an angular correlation between energy landscape features and kinetic friction. The observed ultralow friction regime is consistent with previous reports on other vdW heterostructures, including twisted graphene,[38] MoS_2,[10] and heterogeneous structures,[13] where complete lattice mismatch leads to an ultra-flat PES through destructive interference of atomic corrugations.

Notably, the residual energy barriers at small twist angles ($\theta < 2°$; $\theta > 58°$) originate from structural buckling in Ba_2N bilayers. Our analysis identifies two competing mechanisms: 1) out-of-plane buckling amplitudes (B), quantified as the maximum z-axis displacement difference within atomic layers, and 2) the in-plane perfect domain size (L_P), determined by the lateral distance between two adjacent lowest-energy stacking configurations (Figure 3c,d). Figure 4d depicts the relationships between the twist angle (θ), sliding energy barrier (ΔE_{max}), in-plane perfect domain size (L_P), and out-of-plane buckling amplitude (B) for small twist angles ($1° < \theta < 2°$). For $\theta < 2°$, both ΔE_{max} and B display monotonic decreases with increasing L_P and θ. The observed inverse correlation demonstrates that contraction of the in-plane perfect domain imposes geometric constraints on the out-of-plane deformations, suppressing out-of-plane atomic displacements during friction and thereby reducing PES corrugation. When the twist angle exceeds 2°, the out-of-plane buckling amplitudes diminish below 0.05 Å, inducing a rigid incommensurate lattice behavior in bilayer systems. This transition drives the PES to its global minimum, marking the onset of structural superlubricity. For practical applications, stringent angular control ($\theta > 2°$ misalignment) is required to preserve incommensurate interfaces while avoiding spontaneous reconstruction into commensurate domains. Notably, the identified twist angles ($2° < \theta < 58°$) are experimentally accessible. Recent advances in twisted vdW heterostructure fabrication, such as mechanical transfer method,[43,44] and chemical vapor deposition (CVD) method,[45–47] enable precise control of twisted angles and support the practical relevance of our predictions.

4. Inducing Superlubricity in 2D Electrides through Commensurate Contact

Moreover, the exceptional frictional dynamics of pristine Ba_2N bilayers ($\theta = 0°$) attracted our interest, exhibiting an ultralow shear strength of 4 MPa (Figure 4c), which is substantially lower than the intrinsic shear strength of AB-stacked graphite of 62 MPa.[48] These properties endow Ba_2N with significant potential for applications in nanomechanical systems and superlubricity-enabled materials. The ultralow friction behavior originates from the synergistic effect of a zigzag-type sliding pathway. As illustrated in **Figure 5a**, the periodic evolution of the centroid of the sliding layer along the x-direction (normalized to the lattice constant a) exhibits quantized transitions in increments of $0.5a$, indicating movement along energy-minimized paths. By consistently following these minimum-energy trajectories, the system effectively avoids large-scale energy dissipation, thereby enabling ultralow friction during sliding.

Given the prevalence of high-load conditions in practical tribological interfaces, we further investigated the frictional behavior of Ba_2N under applied normal loads. To monitor the energy variations at the origin of friction, we performed first-principles calculations to track the load-dependent energy difference (ΔE) between AB and AA stacking configurations, corresponding to the maximum and minimum of the sliding PES, respectively. Figure 5b,c shows the tribological behavior of commensurate Ba_2N bilayers ($\theta = 0°$) under varying normal loads, revealing two distinct friction regimes.

Regime I (0 - 2.3 GPa): The shear strength demonstrates a counterintuitive reduction with increasing normal load (Figure 5b), while DFT calculations reveal that the energy barrier ΔE initially increases weakly (Figure 5c). This contradiction can be attributed to the evolution of the PES. Under load-free conditions, the bilayer tends to bypass AB stacking and slide along the zigzag-type minimum energy path (Figure 5a). The system actually have to overcome the transition-state energy barrier between two AA stackings. With increasing normal load, the PES undergoes dynamic evolution (manifested as a reduction in saddle-point energy), consequently resulting in a reduction of the shear strength. At a critical load of 2.1 GPa (defined as the pressure where the energies of AA and AB stacking configurations are equal), ΔE vanishes completely, marking the system's transition to a metastable state with barrier-free sliding potential. Meanwhile, the ratio between the shear strength and the normal load reaches 0.001, which is <0.01, which is usually referred to as the superlubricity threshold.[49] Regime II (> 2.3 GPa): Beyond the critical load, ΔE resurges with inverted polarity (Figure 5c), indicating a fundamental inversion of the stacking stability hierarchy—the formerly high-energy AB configuration becomes energetically favorable. This inversion drives the restored positive correlation between the shear strength and load (Figure 5b), accompanied by a linear growth of $|\Delta E|$.

First-principles charge density difference analysis (Figure 5d) unveils topological reconstruction of interlayer electron clouds under high loads. At ambient pressure (0 GPa), both AA and AB stacking configurations exhibit moderate charge redistribution. The AA stacking configuration exhibits significantly enhanced interlayer electron accumulation (ρ_{redist} = 0.333 e$^-$ Å^{-3}) compared to AB stacking (ρ_{redist} = 0.329 e$^-$ Å^{-3}), as evidenced by the spatially extended red isosurfaces in the interlayer region. This electronic enrichment enhances interlayer Coulomb repulsion through charge compensation effects, resulting in an energetically favorable state with 0.95 meV Å^{-2} lower total energy than AB stacking. Under 2.3 GPa compression, dramatic electronic reconstruction emerges: For AA stacking, intensified charge accumulation develops at interfacial coordination zone, forming an anisotropic electron sphere that spans interlayer gap. For AB stacking, pressure induces asymmetric charge polarization, with alternating accumulation/depletion domains aligning along the shear direction. This distinct behavior can be attributed to the different nitrogen alignments: in AA stacking, the vertically aligned N atoms create symmetric interfacial electric fields that reinforce directional charge confinement, whereas in AB stacking, the staggered N positions induce competing dipole interactions that drive directional charge redistribution. Notably,

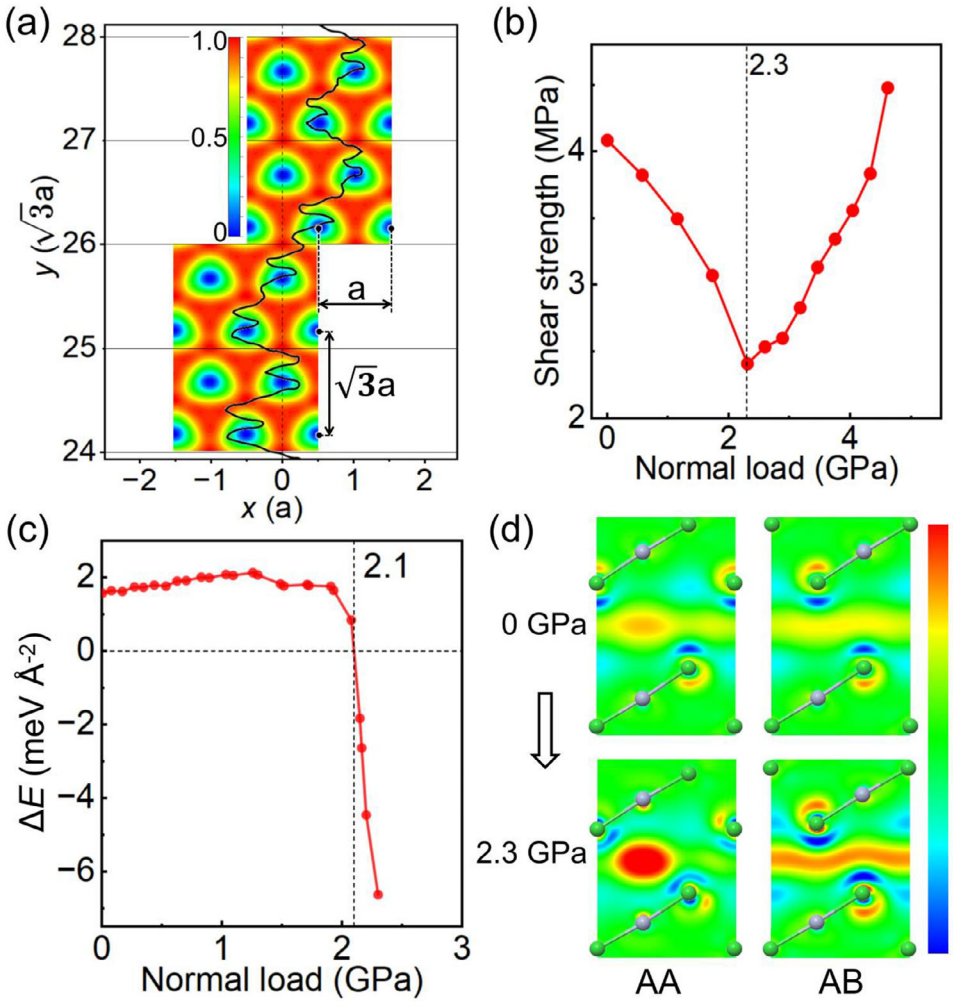

Figure 5. a) Evolution of the centroid's x and y coordinates of sliding layer (normalized by the lattice parameters a and $\sqrt{3}a$, respectively) under load-free conditions (initial position set to (0,0)). The curve shows a zigzag-type sliding path mapping on the PES (meV Å^{-2}). b) Lateral shear strength as a function of the normal load. c) The Energy difference (ΔE) between AB and AA stacking configurations as a function of the normal load. d) The Difference charge density map on the (110) crystallographic plane of Ba_2N bilayer for AA and AB stacking configurations under 0 and 2.3 GPa. The isosurfaces range from −0.002 (blue, charge depletion) to 0.002 (red, charge accumulation) (units: e$^-$ Å^{-3}). The green and gray spheres represent Ba and N atomic positions, respectively.

interfacial charge forms novel charge-compensation channels (red filaments between layers), geometrically matching the sliding pathway observed in barrier-free sliding regime, which effectively screens the interlayer Coulomb repulsion. The difference in the charge density quantitatively demonstrates a pressure-induced inversion of the charge transfer hierarchy, with the AA stacking configuration exhibiting lower interlayer electron accumulation (ρ_{redist} = 0.353 e$^-$ Å^{-3}) compared to the AB stacking (ρ_{redist} = 0.397 e$^-$ Å^{-3}). This electronic inversion correlates directly with the metastable stacking state transition observed in Figure 5c, confirming that pressure-tuned charge redistribution governs the interlayer interaction potential landscape. This frictional collapse behavior is also observed in rare gas/metals and MoS_2 vdW friction systems.[6,50]

Unlike incommensurate systems ($2° < \theta < 58°$) where friction reduction originates from disordered moiré patterns, the Ba_2N commensurate bilayer maintains long-range crystallographic order while achieving complete energy corrugation elimination. The robustness of this state is further enhanced by the strong interlayer adhesion of electrides, which prevents exfoliation under shear stress, a common failure mode in weakly bonded vdW materials. By preserving crystallographic alignment, this mechanism enables precise control over interfacial properties without sacrificing mechanical stability. The observed metastable barrier elimination at critical loading demonstrates a unique pathway for achieving load-adaptive superlubricity in electrides, distinct from conventional structural lubricity mechanisms. Notably, extremely high pressures (of 2.3 GPa) can be present at nano-asperity contacts.[51] Therefore, even in ordinary tribological experiments carried out at lower nominal Hertzian pressure, the local pressure at asperity contact can reach the estimated values for observing the non-Amontonian behavior predicted by our calculations. These findings establish electrides as a promising platform for designing pressure-responsive

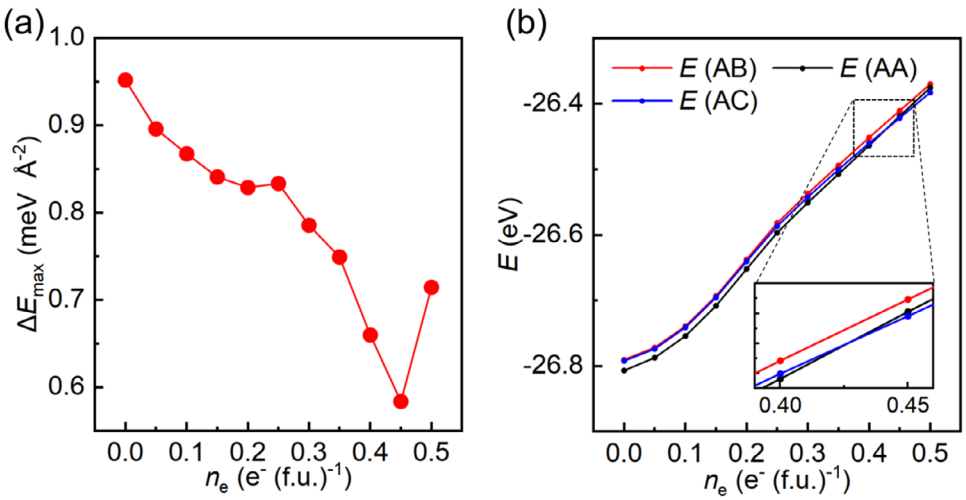

Figure 6. a) Variation of the sliding energy barrier (ΔE_{max}) for bilayer Ba_2N as a function of the number of doping electrons (n_e). b) Energies of the stacking configurations AB, AA, and AC for bilayer Ba_2N as a function of n_e. The inset in (b) highlights that the energy of the AC stacking configuration becomes lower than that of the most stable AA configuration at $n_e \approx 0.45$ e$^-$ (f.u.)$^{-1}$.

smart tribological systems with ultralow friction under extreme loading conditions.

5. Tuning the Friction of 2D Electrides through Electron Doping

Figures 2d and 5d suggest that reducing the interlayer charge redistribution can mitigate the energy barrier associated with the stacking configuration displacement. To explore this phenomenon further, we examine the impact of electron doping on the frictional properties of 2D electrides by varying the electron concentration in the bilayer Ba_2N model. The sliding energy barrier (ΔE_{max}) of bilayer Ba_2N, calculated for electron doping levels ranging from 0 to 0.5 e$^-$ (f.u.)$^{-1}$, is presented in **Figure 6a**. It can be observed that, as n_e increases, ΔE_{max} initially decreases significantly, indicating a pronounced sensitivity to electron doping. However, ΔE_{max} reaches a minimum of 0.58 meV Å^{-2} at $n_e \approx$ 0.45 e$^-$ (f.u.)$^{-1}$, after which it begins to increase as n_e continues to increase.

We further investigated the impact of electron doping on the stacking configurations of bilayer Ba_2N. Figure 6b shows the energies of different stacking configurations—AB, AA, and AC—as a function of the doping electron concentration (n_e), where E(AB), E(AA), and E(AC) correspond to the energies of the AB, AA, and AC stacking configurations, respectively. The initial sliding energy barrier is defined by the energy difference between AA and AB. As n_e increases from 0 to 0.5 e$^-$ (f.u.)$^{-1}$, the stacking energies of all three configurations increase monotonically. Notably, the energy difference between AA and AB decreases, while the energy difference between AC and AB increases. Interestingly, when n_e reaches ≈0.43 e$^-$ (f.u.)$^{-1}$, the energy curves of AA and AC intersect, causing the sliding energy barrier to shift to the energy difference between AC and AB, which continues to rise with further electron doping. The intersection in Figure 6b implies an exchange in the energy ordering between stacking configurations, analogous to frictional collapse behaviors observed in gas/metal and MoS_2 vdW systems.[6,50] Notably, the influence of electron doping on the frictional properties of Ba_2N can also be observed using a bulk model (Figures S9 and S10, Supporting Information), providing further evidence for the modulation of friction in 2D electrides. Our findings offer a deeper understanding of the factors that influence stacking configurations in 2D electrides, suggesting that fine-tuning the electron doping concentration could enable control over the preferred stacking motifs and, consequently, the frictional properties of materials. To introduce additional electrons into the Ba_2N lattice, one could either apply an external electrostatic field to modulate the Fermi level,[52] or substitute heteroatoms for nitrogen atoms in the Ba_2N lattice.[53] The doping-induced friction reduction suggests potential applications in adaptive lubrication systems where friction coefficients can be dynamically tuned through electrostatic gating,[52] creating smart interfaces responsive to operational conditions.

6. Conclusion

In summary, we have investigated the tribological properties of 2D electrides using ab initio and DPMD calculations. We uncovered the mechanism of atomic-scale friction within these 2D electride systems, considering both structural and electronic factors. The sliding energy barriers of 2D electrides correlate with the Coulombic repulsion difference between the maximum and minimum energy stacking configurations. Contrary to the prevailing belief that systems with high interlayer binding energy exhibit poor lubrication properties, the sliding energy barrier for Ba_2N is about three times smaller than that of graphite, though the adhesion energy is significantly higher.

DPMD simulations reveal that incommensurate contact configurations in Ba_2N bilayers demonstrate significantly reduced shear strength (<0.5 MPa). Remarkably, commensurate contact systems under an extra critical pressure (2.3 GPa) exhibit superlubricity, with the ratio between the shear strength and the normal load reaching 0.001. Finally, by leveraging the pivotal role of interlayer electrons, friction in 2D electrides can be significantly reduced through electron doping. These findings highlight the

interplay between the tribological, structural, and electronic properties of 2D electrides. They highlight incommensurate contact, commensurate contact, and electron doping as effective strategies for reducing friction in these materials, offering significant potential for cost-efficient fabrication and practical engineering applications.

7. Experimental Section

Ab initio Calculations: The ab initio calculations were performed based on density functional theory (DFT)[54] using the projector-augmented wave method as implemented in the Vienna *Ab-initio* Simulation Package (VASP).[55,56] The exchange-correlation energy was modeled using the generalized gradient approximation (GGA) of Perdew, Burke, and Ernzerhof (PBE).[57] Long-range vdW interactions were added using Grimme's DFT-D3 approach.[58] The wavefunctions were expanded on a plane-wave basis set with a cutoff energy of 520 eV. The Brillouin zone was sampled using an $11 \times 11 \times 11$ k-point mesh. Before calculating the static potential energy surface (PES), all atoms were completely relaxed until the forces were <10 meV Å^{-1}. The initial data set was generated from ab initio molecular dynamics (AIMD) simulations, which were performed in the canonical (NVT), where the number of particles (N), volume (V), and temperature (T) are kept constant ensembles, with Nosé–Hoover thermostats.[59,60]

Bader Charge Analysis: The Bader method considers the zero-flux surface of the charge density to divide the molecular space into atomic volumes known as Bader basins.[29,30] In electrides, the volume of the Bader basin around the interlayer anionic electrons where the electron density is maximum, known as a non-nuclear attractor, is estimated to be an empty sphere (pseudo atom). The central coordinates of the interlayer anionic electrons are all (0, 0, 0.5), which are determined semi-empirically in the unit cell by examining the electron localization function (ELF) regions separated from the atoms (Figure S1, Supporting Information). Here, the Bader charge analysis was carried out using the pre-converged total charge density with reference to the projected charge density, which employs a substitution of pseudo atom for interlayer anionic electrons.

MLFF Model Training: DeePMD-kit software[39,40] was used to fit the neural network for atomic interactions within a deep learning framework. The embedding network employed had three hidden layers with 25, 50, and 100 nodes, respectively, while the fitting network used three hidden layers, each with 240 nodes. A cutoff radius of 7.0 Å was applied. The learning rate decayed exponentially from 0.001 every 2000 steps, eventually reaching 3.51×10^{-8} after 1 000 000 training steps, with start and limit scaling factors of energy and force set at 0.02, 1, 1000, and 1, respectively.

Deep Potential Molecular Dynamics: All DPMD simulations based on MLFF were performed using Large-scale Atomic/Molecular Massively Parallel Simulator (LAMMPS)[61] in the NVT ensemble. Periodic boundary conditions were applied in the *x* and *y* directions, whereas non-periodic and fixed boundary conditions were applied in the *z* direction. The time step was set to 1 fs. The conjugate gradient (CG) energy minimization method with a force criterion of 10^{-12} eV Å^{-1} was used to pre-equilibrate the initial models. Trajectory analyses were performed with OVITO software.[62]

Supporting Information

Supporting Information is available from the Wiley Online Library or from the author.

Acknowledgements

This work was supported by the National Key Research and Development Program of China (2023YFB3003005). MCR gratefully acknowledges the ERC-SLIDE project (Grant agreement No. 865633).

Conflict of Interest

The authors declare no conflict of interest.

Data Availability Statement

The data that support the findings of this study are available in the Supporting Information of this article.

Keywords

2D electrides, deep potential molecular dynamics, electron redistribution, superlubricity, twisted interfaces, ultralow friction

Received: September 28, 2025
Revised: November 11, 2025
Published online: November 24, 2025

[1] K. Holmberg, A. Erdemir, *FME Trans.* **2015**, *43*, 181.
[2] F. He, G. Xie, J. Luo, *Friction* **2020**, *8*, 4.
[3] M. Dienwiebel, G. S. Verhoeven, N. Pradeep, J. W. M. Frenken, J. A. Heimberg, H. W. Zandbergen, *Phys. Rev. Lett.* **2004**, *92*, 126101.
[4] M. H. Müser, *Europhys. Lett.* **2004**, *66*, 97.
[5] S. Liu, H. Wang, Q. Xu, T. Ma, G. Yu, C. Zhang, D. Geng, Z. Yu, S. Zhang, W. Wang, Y. Hu, H. Wang, J. Luo, *Nat. Commun.* **2017**, *8*, 14029.
[6] M. C. Righi, M. Ferrario, *Phys. Rev. Lett.* **2007**, *99*, 176101.
[7] J. Sun, Y. Zhang, Z. Lu, Q. Xue, L. Wang, *Phys. Chem. Chem. Phys.* **2017**, *19*, 11026.
[8] Z. Cheng, H. Feng, J. Sun, Z. Lu, Q. He, *Adv. Mater. Interfaces* **2023**, *10*, 2202062.
[9] B. Jiang, Z. Zhao, Z. Gong, D. Wang, G. Yu, J. Zhang, *Appl. Surf. Sci.* **2020**, *520*, 146303.
[10] H. Li, J. Wang, S. Gao, Q. Chen, L. Peng, K. Liu, X. Wei, *Adv. Mater.* **2017**, *29*, 1701474.
[11] R. Li, X. Yang, D. Hou, Y. Wang, J. Zhang, *Mater. Lett.* **2020**, *271*, 127748.
[12] K. C. Mutyala, G. L. Doll, J. Wen, A. V. Sumant, *Appl. Phys. Lett.* **2019**, *115*, 103103.
[13] Y. Song, D. Mandelli, O. Hod, M. Urbakh, M. Ma, Q. Zheng, *Nat. Mater.* **2018**, *17*, 894.
[14] W. Wang, G. Xie, J. Luo, *ACS Appl. Mater. Interfaces* **2018**, *10*, 43203.
[15] S. Yi, J. Li, Y. Liu, X. Ge, J. Zhang, J. Luo, *Tribol. Int.* **2021**, *154*, 106695.
[16] J. S. Choi, J. Kim, I. Byun, D. H. Lee, M. J. Lee, B. H. Park, C. Lee, D. Yoon, H. Cheong, K. H. Lee, Y. Son, J. Y. Park, M. Salmeron, *Science* **2011**, *333*, 607.
[17] Q. Li, C. Lee, R. W. Carpick, J. Hone, *phys. status solidi* **2010**, *247*, 2909.
[18] K. Kim, H. Lee, C. Lee, S. Lee, H. Jang, J. Ahn, J. Kim, H. Lee, *ACS Nano* **2011**, *5*, 5107.
[19] L. Liu, Y. Li, H. Wang, Z. Yang, K. Wang, J. Luo, Y. Liu, *Mater. Sci. Eng.: R: Rep.* **2024**, *161*, 100868.
[20] T. Inoshita, S. Jeong, N. Hamada, H. Hosono, *Phys. Rev. X* **2014**, *4*, 031023.
[21] K. Lee, S. W. Kim, Y. Toda, S. Matsuishi, H. Hosono, *Nature* **2013**, *494*, 336.
[22] A. Walsh, D. O. Scanlon, *J. Mater. Chem. C* **2013**, *1*, 3525.
[23] D. L. Druffel, K. L. Kuntz, A. H. Woomer, F. M. Alcorn, J. Hu, C. L. Donley, S. C. Warren, *J. Am. Chem. Soc.* **2016**, *138*, 16089.
[24] S. S. Batsanov, *Inorg. Mater.* **2001**, *37*, 871.
[25] S. Yi, J. Choi, K. Lee, S. W. Kim, C. H. Park, J. Cho, *Phys. Rev. B* **2016**, *94*, 235428.

[26] Z. Zhang, Y. Jiang, J. Li, M. Miyazaki, M. Kitano, H. Hosono, *J. Am. Chem. Soc.* **2023**, *145*, 24482.
[27] W. Ming, M. Yoon, M. Du, K. Lee, S. W. Kim, *J. Am. Chem. Soc.* **2016**, *138*, 15336.
[28] T. Tada, S. Takemoto, S. Matsuishi, H. Hosono, *Inorg. Chem.* **2014**, *53*, 10347.
[29] W. Tang, E. Sanville, G. Henkelman, *J. Phys.: Condens. Matter* **2009**, *21*, 084204.
[30] M. Yu, D. R. Trinkle, *J. Chem. Phys.* **2011**, *134*, 064111.
[31] M. Wolloch, G. Levita, P. Restuccia, M. C. Righi, *Phys. Rev. Lett.* **2018**, *121*, 026804.
[32] P. Restuccia, G. Levita, M. Wolloch, G. Losi, G. Fatti, M. Ferrario, M. C. Righi, *Comput. Mater. Sci.* **2018**, *154*, 517.
[33] M. Reguzzoni, A. Fasolino, E. Molinari, M. C. Righi, *Phys. Rev. B* **2012**, *86*, 245434.
[34] S. Cahangirov, S. Ciraci, V. O. Özçelik, *Phys. Rev. B* **2013**, *87*, 205428.
[35] L. Wang, X. Zhou, T. Ma, D. Liu, L. Gao, X. Li, J. Zhang, Y. Hu, H. Wang, Y. Dai, J. Luo, *Nanoscale* **2017**, *9*, 10846.
[36] J. Sun, X. Zhang, S. Du, J. Pu, Y. Wang, Y. Yuan, L. Qian, J. S. Francisco, *J. Am. Chem. Soc.* **2023**, *145*, 5536.
[37] X. Zhang, J. Sun, S. Du, H. Li, L. Qian, *Adv. Funct. Mater.* **2023**, *33*, 2301402.
[38] M. Hirano, K. Shinjo, *Phys. Rev. B* **1990**, *41*, 11837.
[39] H. Wang, L. Zhang, J. Han, W. E, *Comput. Phys. Commun.* **2018**, *228*, 178.
[40] J. Zeng, D. Zhang, D. Lu, P. Mo, Z. Li, Y. Chen, M. Rynik, L. a. Huang, Z. Li, S. Shi, Y. Wang, H. Ye, P. Tuo, J. Yang, Y. Ding, Y. Li, D. Tisi, Q. Zeng, H. Bao, Y. Xia, J. Huang, K. Muraoka, Y. Wang, J. Chang, F. Yuan, S. L. Bore, C. Cai, Y. Lin, B. Wang, J. Xu, et al., *J. Chem. Phys.* **2023**, *159*, 054801.
[41] X. Liu, R. Peng, Z. Sun, J. Liu, *Nano Lett.* **2022**, *22*, 7791.
[42] R. He, B. Zhang, H. Wang, L. Li, P. Tang, G. Bauer, Z. Zhong, *Acta Mater.* **2024**, *262*, 119416.
[43] V. Carozo, C. M. Almeida, E. H. M. Ferreira, L. G. Cançado, C. A. Achete, A. Jorio, *Nano Lett.* **2011**, *11*, 4527.
[44] K. Kim, M. Yankowitz, B. Fallahazad, S. Kang, H. C. P. Movva, S. Huang, S. Larentis, C. M. Corbet, T. Taniguchi, K. Watanabe, S. K. Banerjee, B. J. LeRoy, E. Tutuc, *Nano Lett.* **2016**, *16*, 1989.
[45] L. Sun, Z. Wang, Y. Wang, L. Zhao, Y. Li, B. Chen, S. Huang, S. Zhang, W. Wang, D. Pei, H. Fang, S. Zhong, H. Liu, J. Zhang, L. Tong, Y. Chen, Z. Li, M. H. Rümmeli, K. S. Novoselov, H. Peng, L. Lin, Z. Liu, *Nat. Commun.* **2021**, *12*, 2391.
[46] S. Liu, B. He, W. Yang, X. Zhou, X. Xue, M. Liu, Y. Zhao, X. Wang, J. Si, F. Wang, Z. Zhang, L. Peng, G. Yu, *Adv. Mater.* **2024**, *36*, 2312125.
[47] M. Liu, S. Wang, H. Huang, X. Xue, X. Zhou, Z. Chen, S. Liu, X. Liu, J. Dong, W. Niu, Y. Liu, L. Wang, G. Yu, *Adv. Mater.* **2025**, *37*, 2506242.
[48] Y. Wang, S. Feng, D. Peng, T. Li, C. Zheng, Z. Cai, Z. Wu, Q. Zheng, Z. Xu, *J. Mech. Phys. Solids* **2024**, *193*, 105853.
[49] D. Berman, A. Erdemir, A. V. Sumant, *ACS Nano* **2018**, *12*, 2122.
[50] J. Sun, Y. Zhang, Z. Lu, Q. Li, Q. Xue, S. Du, J. Pu, L. Wang, *J. Phys. Chem. Lett.* **2018**, *9*, 2554.
[51] B. Demirkurt, D. Petrova, D. K. Sharma, M. Vacha, B. Weber, D. Bonn, A. M. Brouwer, *J. Phys. Chem. Lett.* **2024**, *15*, 1936.
[52] A. Das, S. Pisana, B. Chakraborty, S. Piscanec, S. K. Saha, U. V. Waghmare, K. S. Novoselov, H. R. Krishnamurthy, A. K. Geim, A. C. Ferrari, A. K. Sood, *Nat. Nanotechnol.* **2008**, *3*, 210.
[53] H. Zhu, X. Gan, A. McCreary, R. Lv, Z. Lin, M. Terrones, *Nano Today* **2020**, *30*, 100829.
[54] P. Hohenberg, W. Kohn, *Phys. Rev.* **1964**, *136*, B864.
[55] P. E. Blöchl, *Phys. Rev. B* **1994**, *50*, 17953.
[56] G. Kresse, J. Furthmüller, *Phys. Rev. B* **1996**, *54*, 11169.
[57] J. P. Perdew, M. Ernzerhof, K. Burke, *J. Chem. Phys.* **1996**, *105*, 9982
[58] T. Bučko, J. Hafner, S. Lebègue, J. G. Ángyán, *J. Phys. Chem. A* **2010**, *114*, 11814.
[59] W. G. Hoover, *Phys. Rev. A* **1985**, *31*, 1695.
[60] S. Nosé, *J. Chem. Phys.* **1984**, *81*, 511.
[61] A. P. Thompson, H. M. Aktulga, R. Berger, D. S. Bolintineanu, W. M. Brown, P. S. Crozier, P. J. in 't Veld, A. Kohlmeyer, S. G. Moore, T. D. Nguyen, R. Shan, M. J. Stevens, J. Tranchida, C. Trott, S. J. Plimpton, *Comput. Phys. Commun.* **2022**, *271*, 108171.
[62] A. Stukowski, *Modell. Simul. Mater. Sci. Eng.* **2010**, *18*, 015012.